Journal of Power Sources 342 (2017) 351–362

Contents lists available at ScienceDirect

Journal of Power Sources

journal homepage: www.elsevier.com/locate/jpowsour

Continuous piecewise-linear, reduced-order electrochemical model for lithium-ion batteries in real-time applications

Mohammed Farag [a, *, 1], Matthias Fleckenstein [b], Saeid Habibi [a]

[a] McMaster University, Department of Mechanical Engineering, Center of Mechatronics and Hybrid Technologies CMHT, L8S4L8, Ontario, Canada
[b] BMW Group, Battery Technology, 80788, Munich, Germany

HIGHLIGHTS

- An improvement of the single particle model using piecewise linearization technique.
- Optimal knot-placement algorithm for continuous piecewise-linear models.
- Model parameters dependencies on the electrode's state of charge.
- Experimental validation of the model for automotive operating conditions.
- The computational cost (CPU run-time) is highly reduced while maintaining accuracy.

ARTICLE INFO

Article history:
Received 6 June 2016
Received in revised form
5 September 2016
Accepted 12 December 2016

Keywords:
Lithium-ion battery
Electrochemical modeling
Model parameterization
Piecewise linearization
Knot placement
Battery management system

ABSTRACT

Model-order reduction and minimization of the CPU run-time while maintaining the model accuracy are critical requirements for real-time implementation of lithium-ion electrochemical battery models. In this paper, an isothermal, continuous, piecewise-linear, electrode-average model is developed by using an optimal knot placement technique. The proposed model reduces the univariate nonlinear function of the electrode's open circuit potential dependence on the state of charge to continuous piecewise regions. The parameterization experiments were chosen to provide a trade-off between extensive experimental characterization techniques and purely identifying all parameters using optimization techniques. The model is then parameterized in each continuous, piecewise-linear, region. Applying the proposed technique cuts down the CPU run-time by around 20%, compared to the reduced-order, electrode-average model. Finally, the model validation against real-time driving profiles (FTP-72, WLTP) demonstrates the ability of the model to predict the cell voltage accurately with less than 2% error.

1. Introduction

In the past few years, automobile manufacturers have gone through the initial adoption phase of electric mobility. The gradually increasing momentum behind electric vehicles (EV) adoption suggests that electrified storage systems will play an important role in electric mobility going forward. Lithium ion batteries have become one of the most attractive alternatives for electric vehicles' energy storage systems due to their light weight, high specific energy, low self-discharge rate, and non-memory effect, etc. [1]. To fully benefit from a lithium-ion energy storage system and avoid its physical limitations, an accurate battery management system (BMS) is required. In EV, the BMS is responsible for performance management which includes -but is not limited to-state of charge (SOC), state of health (SOH), and state of function (SOF) estimation algorithms, as well as power management, thermal management, and so forth. One of the key issues for successful BMS implementation is the battery model. A robust, accurate, and high fidelity battery model is required to mimic the battery dynamic behavior in a harsh environment.

In the literature, numerous battery models have been reported. The choice between these models is a trade-off between model complexity, accuracy, and parameterization effort. The models can be classified into three categories of increasing complexity: behavioral (or black-box) [2–5], equivalent circuit [6–9], and finally detailed electrochemical (physics-based) models. Currently,

* Corresponding author. McMaster University, JHE 316-1280 Main Street West, L8S 4L8 Hamilton, Ontario, Canada.
E-mail address: faragms@mcmaster.ca (M. Farag).
[1] https://www.linkedin.com/in/mohammedfarag.

http://dx.doi.org/10.1016/j.jpowsour.2016.12.044
0378-7753/

the equivalent circuit models are commonly used in the BMS because of their low computational complexity and acceptable accuracy. However, they are not capable of describing the battery's internal physical behavior.

Many approaches to model the electrochemical processes in the battery have been proposed in the literature. Most of the models are derived from the physics-based, electrochemical pseudo-two-dimensional (P2D) model developed by Doyle-Fuller-Newman model [10,11], which is based on the porous electrode and concentrated solution theory. The primary gain of the rigorous physics-based P2D model is the increased accuracy/precision achieved by modeling the electrochemical processes. Unfortunately, it is high in complexity, computational time, memory allocations, and real-time control. Therefore, simplification of the P2D model is required. In the literature, numerous reduction methods have been explored, all of which have the goal of reducing the computational complexity involved in solving the physics-based electrochemical model while maintaining acceptable accuracy.

These methods can be divided into two categories. The first one is primarily focused on reducing the computational complexity involved in solving for the concentration of lithium in the solid particles of the electrodes, e.g. Subramanian et al. [12–14] developed a simplified model using the Liapunov-Schmidt technique, perturbation techniques, volume averaging, and intuition-based simplifications. Their approach works well at low-to-moderate discharge rates but performs poorly for highly dynamic current profiles such as those encountered in hybrid- and electric-vehicle applications. Cai et al. [15] proposed an approach based on proper orthogonal decomposition, which uses a two-step approximation of the full order model; The first approximation is discretizing the governing equations and the second is truncating the number of orthogonal modes. The proposed reduced order model proved to be about seven times faster than the full order model. Forman et al. [16] used quasi-linearization and Padé approximation. This approach uses a quasi-linearized model of intercalation current to solve the model algebraic equations, then a Padé approximation of spherical diffusion is used to decrease the model complexity while maintaining a high level of accuracy. Wang et al. [17] assumed a parabolic concentration profile within the spherical particle ($c_s = a_0 + a_1 r + a_2 r^2$) formulating a solid state diffusion submodel, which correctly captures bulk dynamics and steady state concentration gradient but otherwise neglects diffusion dynamics. It is, therefore, valid for extended operation times and low C-rates, as its inaccuracies become significant at higher C-rates. Smith et al. [18,19] proposed a simplified model using the method of residue grouping. They used a nonlinear optimization technique to minimize the error in the frequency domain response between the 'full order' and 'reduced order' model. The derived transfer functions are represented by a truncated series of grouped residues with similar eigenvalues. Bhikkaji et al. [20,21] developed a simplified model based on Chebyshev polynomial.

The second category of model simplification is focused on reducing the electrochemical model as a whole. The primary contribution pertains to avoiding the solution of large sets of differential-algebraic equations (DAEs) of the Li^+ concentration distribution and the potential distribution of the electrolyte phase. This provides a reduced model capable of computing in real-time. However, this strategy for model simplification leads to loss of information. The performance reduces at higher C-rates in comparison to the full order model. In general, the assumptions used for the model reduction can lead to inaccuracies if a broad C-rate range of operation is considered and if the model is not adjusted with respect to the operating conditions of the battery. Examples of this modeling approach, Haran et al. [22] originally developed the single particle model (SPM) approach for the metal hydride battery, and it was extended to the lithium system by Santhanagopalan in Refs. [23,24]. In this model, the local volumetric current density j^{li} is constant across the electrode (anode or cathode) and equal to an average value $\bar{j}^{li}$. Rahimian et al. [25] extended the SPM by including a polynomial approximation of the electrolyte dynamics. Domenico et al. [26] presented the electrode averaging model (EAM). In literature, there are also other methodologies reported for solving the original physics-based P2D model directly.

This paper contributes to the literature above by developing three unique improvements to the reduced-order electrode average electrochemical model presented by Domenico et al. [26]. The first contribution is a continuous piecewise linearized (CPWL) technique that aids in efficiently running the model in real time applications. The second contribution is an optimal knot-placement optimization technique for the continuous piecewise linearized electrode averaged model (CPWL-EAM) using the genetic algorithm (GA). The third contribution is a parameter-grouping approach that helps in reducing the parameterization efforts for the EAM and the CPWL-EAM. First, the optimal knot locations are obtained using the GA to minimize the residual error. The CPWL-EAM parameters are then identified in order to minimize the error between the model terminal voltage output and the experimental data. The model is then validated using battery voltage, current, and temperature measurements against real-time driving cycles.

Paper structure. First, the full-order electrochemical model is briefly introduced. Next, the continuous piecewise linearization technique is presented. Then, the battery parameter identification procedure and the experimental setup are illustrated. The model validation against two different real-time driving cycles is then shown. Finally, the results and discussion are presented.

2. Electrochemical battery modeling

2.1. Operating principles of lithium-ion batteries

A battery converts chemical energy into electrical energy and vice versa. The basic setup of a battery cell consists of four main parts: the positive electrode, the separator, the electrolyte, and the negative electrode, as shown in Fig. 1.

The positive and negative electrodes are referred to as the cathode and the anode. The battery is connected to an external load using current collector plates. In the case of Li-ion cells, a copper collector is used in the negative electrode while an aluminum collector is used for the positive electrode.

The anode is the electrode capable of supplying electrons to the load. The anode is usually made up of a mixture of carbon (e.g. Li_xC_6), the cathode is typically made of metal oxides (ex. $LiCoO_2$ or $LiMn_2O_4$), while the electrolyte can be made of a salt-containing solvent mixture, polymer, or solid materials (e.g. $LiPF_6$), polymer or solid materials. In the case of solid or polymer materials, the electrolyte will also act as a separator. The separator is a porous membrane allowing the transfer of lithium ions between the electrodes, but which serves as a barrier to electrons. It prevents the occurrence of a short-circuit and thermal run away, while at the same time offering negligible resistance to the flow of ions between the electrodes.

2.2. Model mathematical formulation

2.2.1. Relationship between concentrations and currents

The mathematical equations governing the charge and mass conservation in the solid and electrolyte phases is summarized in this section.

Mass transport in the solid phase. The electrode model is based on the porous electrode theory, and the lithium-ion concentration in a single spherical particle is described by Fick's law of diffusion [24].

$$\frac{\partial c_s^{n,p}(x,r,t)}{\partial t} = \frac{D_s}{r^2}\frac{\partial}{\partial r}\left[r^2\frac{\partial c_s^{n,p}(x,r,t)}{\partial r}\right] \tag{1}$$

where $c_s(x,r,t) : (0,L)\times(0,R_s^{n,p})\times(t_0,t)\rightarrow[0,c_{s,max}^{n,p}]$ is the concentration of Li^+ in the solid particles, as shown in Fig. 1. At the particle surface, the rate at which ions exit or enter the particle is proportional to the volumetric rate of chemical reaction j^{li}, while at the center of the particle the rate is equal to zero, written as the boundary conditions (BC):

$$\left.\frac{\partial c_s^{n,p}}{\partial r}\right|_{r=0} = 0 \quad \text{and} \quad \left.\frac{\partial c_s^{n,p}}{\partial r}\right|_{r=R_s^{n,p}} = \frac{-j^{li}}{D_s a_s F} \tag{2}$$

With initial conditions (IC):

$$c_s^{n,p}(x,r,t_0) = c_{s_0}^{n,p}(x,r) \tag{3}$$

Mass transport in the electrolyte. The Li^+ concentration in the electrolyte changes due to the flow of ions and the current. It can be described by Fick's law of diffusion along the coordinate between the electrodes, with the mass transport between the electrodes treated as being effectively homogeneous at all coordinates in the plane normal to the inter-electrode coordinate.

$$\frac{\partial \varepsilon_e c_e(x,t)}{\partial t} = \frac{\partial}{\partial x}\left(D_e^{eff}\frac{\partial c_e(x,t)}{\partial t}\right) + \frac{1-t_0^+}{F}j^{li} \tag{4}$$

where $c_e(x,t)$ is the concentration of Li^+ in the electrolyte and ε_e and D_e^{eff} are domain-dependent parameters (anode, cathode, separator). The Bruggeman's relation $D_e^{eff} = D_e \times \varepsilon_e^{1.5}$ accounts for the tortuous path of Li^+ transport through the porous electrodes and separator. Ensuring zero flux at the current collector and continuity of concentration and flux through the adjoining domains within the cell, written as boundary conditions:

$$\left.\frac{\partial c_e^n}{\partial x}\right|_{x=0} = 0 \quad \text{and} \quad \left.\frac{\partial c_e^p}{\partial x}\right|_{x=L} = 0 \tag{5}$$

With initial conditions:

$$c_e(x,t_0) = c_{e_0}(x) \tag{6}$$

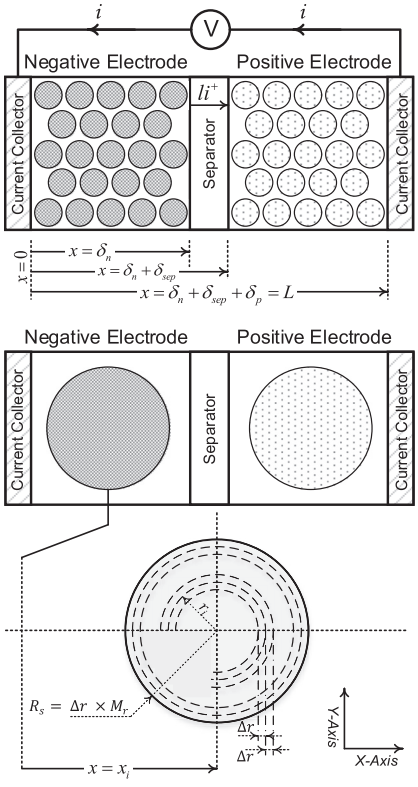

Fig. 1. Schematic representation of the Li-ion battery operation principles and the single particle model simplification.

2.2.2. Relationship between potential and currents

Potential in the solid electrodes. The electrical potential in the electrodes ϕ_s is derived from the extended Ohm's law:

$$\frac{\partial}{\partial x}\left(\sigma^{eff}\frac{\partial}{\partial x}\phi_s(x,t)\right) - j^{li} = 0 \tag{7}$$

The potentials at the current collectors ($x = 0$ and $x = L$) are proportional to the applied current, I and zero at the separator, written as boundary conditions (where A is the cross-sectional area of the cell):

$$\begin{aligned} -\sigma^{eff}\frac{\partial}{\partial x}\phi_s(x,t)\big|_{x=0} &= -\sigma^{eff}\frac{\partial}{\partial x}\phi_s(x,t)\big|_{x=L} = \frac{I}{A} \\ \frac{\partial}{\partial x}\phi_s(x,t)\big|_{x=\delta_n} &= \frac{\partial}{\partial x}\phi_s(x,t)\Big|_{x=\delta_n+\delta_{sep}} = 0 \end{aligned} \tag{8}$$

Potential in the electrolyte. The electrical potential in the electrolyte ϕ_e is derived from the charge conservation law:

$$\frac{\partial}{\partial x}\left(\kappa^{eff}\frac{\partial}{\partial x}\phi_e(x,t)\right) + \frac{\partial}{\partial x}\left(\kappa_D^{eff}\frac{\partial}{\partial x}\ln c_e\right) + j^{li} = 0 \tag{9}$$

With boundary conditions:

$$\frac{\partial}{\partial x}\phi_e(x,t)\big|_{x=0} = \frac{\partial}{\partial x}\phi_e(x,t)\big|_{x=L} = 0 \tag{10}$$

2.2.3. Butler-Volmer kinetics equations

The volumetric rate of chemical reaction is governed by the Butler-Volmer current density equation. This equation links the reaction rate to the phase potentials and is described as:

$$j^{li} = a_s j_0\left[\exp\left(\frac{\alpha_a F}{RT}\eta\right) - \exp\left(-\frac{\alpha_c F}{RT}\eta\right)\right] \tag{11}$$

The overpotential η is defined as the difference between the cell's overpotential and its charge/discharge voltage. It is responsible for driving the electrochemical reaction, and can be calculated as follows:

$$\eta = \phi_s - \phi_e - U(c_{se}) \tag{12}$$

where $U(c_{se})$ is the open circuit potential and the coefficient j_0 is a function of the surface electrolyte concentration c_{se} according to equation (13).

$$j_0 = (c_e)^{\alpha_a}\left(c_{s,\max}^{n,p} - c_{se}^{n,p}\right)^{\alpha_a}\left(c_{se}^{n,p}\right)^{\alpha_c} \tag{13}$$

2.2.4. Cell potential equations

The cell potential, V, across the cell terminals is determined as follows:

$$V = \phi_s(x = L) - \phi_s(x = 0) - R_f \frac{I}{A} \tag{14}$$

The mathematical formulation, describing the full order electrochemical model equations (1)–(14), is presented in Fig. 2.

2.3. Model reduction

The full-order model (FOM) is highly accurate; however it requires extensive computational time and onboard memory allocation, which limits its utility for real-time applications. Therefore, reduction of the FOM has been carried out by simplifying the set of FOM equations for ion concentration and potential in electrode and electrolytes. In this section, some assumptions and simplifications to the FOM are considered in order to obtain a Reduced Order Model (ROM) as shown in Fig. 3.

2.3.1. Model reduction assumptions

The FOM equations represented in equations (1)–(14) are simplified in order to be implemented in real-time applications. The simplification assumptions are summarized in Table 1. As a result of these reductions, a single particle from each electrode (anode and cathode) can describe the diffusion dynamics.

2.3.2. Reduced-order model

The FOM set of equations is simplified due to the previous assumptions. The reduced-order, electrode-averaged model (ROM) is summarized in equation (15)–(19). Its terminal voltage can be calculated by substituting equation (12) in equation (14), as derived in Ref. [24]:

$$V(t) = \left(\overline{\eta}_p - \overline{\eta}_n\right) + \left(\overline{\phi}_e^p - \overline{\phi}_e^n\right) + \left[U_p(\theta_p) - U_n(\theta_n)\right] - R_f \frac{I}{A} \tag{20}$$

where $\overline{\eta}_p - \overline{\eta}_n$ is the difference between the positive and negative electrode overpotentials, and can be calculated by substituting equation (19) in (11) as shown below:

$$\overline{\eta}_p - \overline{\eta}_n = \frac{RT}{\alpha_a F} \ln \frac{\xi_p + \sqrt{\xi_p^2 + 1}}{\xi_n + \sqrt{\xi_n^2 + 1}} \quad where \quad \xi_{n,p} = \frac{\overline{j}_{n,p}^{li}}{2a_s j_0} \tag{21}$$

$\overline{\phi}_e^p - \overline{\phi}_e^n$ is the difference between the positive and negative terminals electrolyte potentials, and can be represented as derived in Ref. [24]:

$$\overline{\phi}_e^p - \overline{\phi}_e^n = -\frac{I}{2A\kappa^{eff}} \left(\delta_n + 2\delta_{sep} + \delta_p\right) \tag{22}$$

Finally, $U_p(\theta_p) - U_n(\theta_n)$ is the difference between the open circuit voltage for the positive and negative electrolyte. The stoichiometry ratio $\theta_{n,p}$ is the normalized solid-electrolyte interface concentration for the negative and positives electrodes respectively.

$$\theta_{n,p} = \frac{\overline{c}_{s,e}^{n,p}}{c_{s,max}^{n,p}} \tag{23}$$

where $\overline{c}_s^{n,p}$ is the average bulk concentration, and can be obtained by calculating the total concentration volumetric average V_s.

$$\overline{c}_s^{n,p}(t) = \frac{1}{V_s} \int_0^{R_{n,p}} c_s^{n,p}(r,t)\, \mathrm{d}V_s \tag{24}$$

2.4. Capacity model mathematical formulation

In this paper, the battery nominal capacity C_{nom} is determined by the mass of active material contained in a fully charged cell. It can be measured by calculating the maximum number of ampere-hours that can be drawn from the fully charged battery at room temperature (293 K) and very low C-rate (C/25). The volumetric averaged Li concentration can be determined by substituting $V_s = 4\pi R_s^3/3$ and $dV_s = 4\pi r^2 dr$ in equation (24).

$$\overline{c}_s^{n,p}(t) = \frac{3}{R_s^3} \int_0^{R_s} r^2 c_s^{n,p}(r,t)\, \mathrm{d}r \tag{25}$$

By using the boundary conditions in equation (2) and

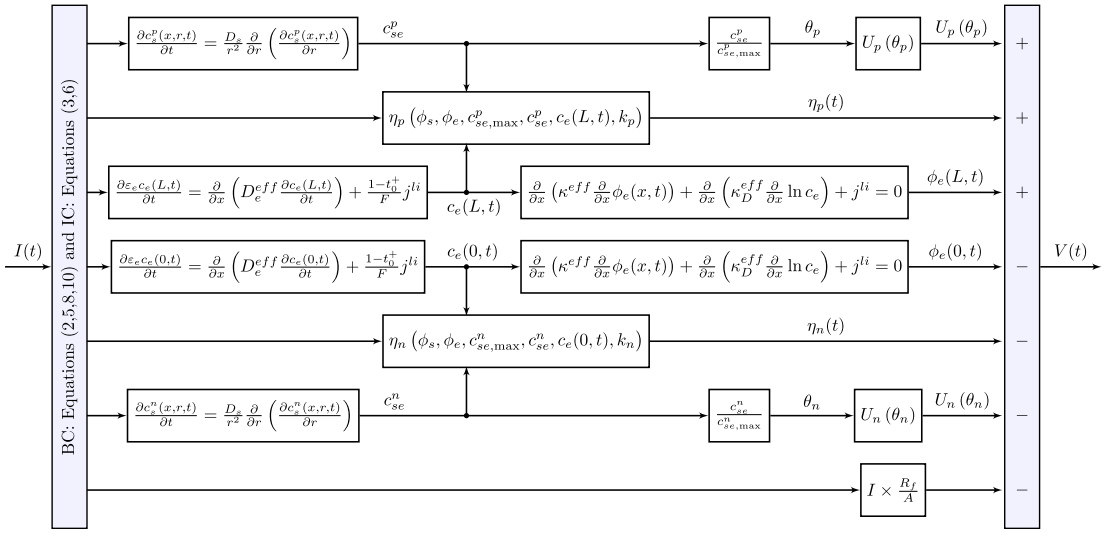

Fig. 2. Block diagram representations for the coupled nonlinear partial differential equations in the full order electrochemical model.

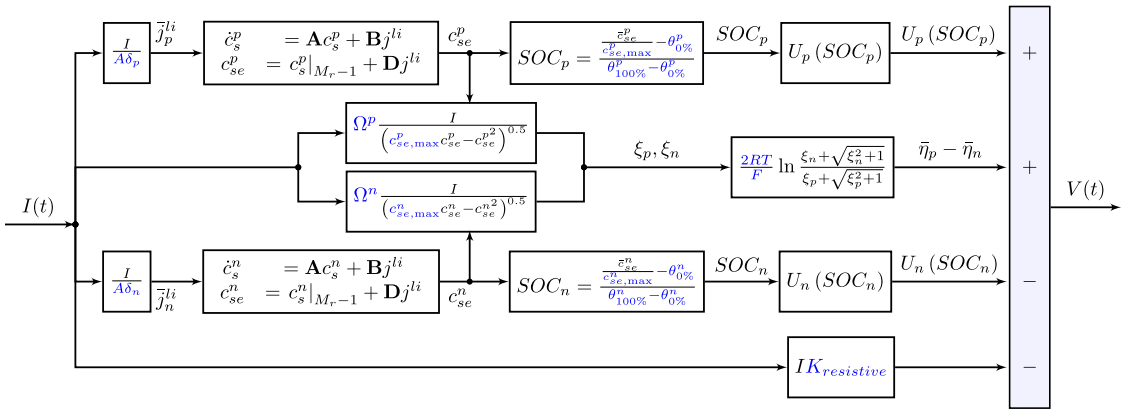

Fig. 3. Block diagram representation for the reduced-order, electrode-average model with $\Omega^{n,p}$ and K_{res}.

substituting equation (19) into equation (2), the volumetric averaged Li concentration dynamics in equation (25) become [27]:

$$\bar{c}_s^{n,p}(t) = \frac{3D_s}{R_s^{n,p}}\left[R_s^{2_{n,p}}\partial c_s\left(R_s^{n,p},t\right)\right] = \frac{I}{\delta_{n,p}A\varepsilon_s^{n,p}F} \tag{26}$$

The state of charge is defined as

$$SOC = \frac{1}{C_{nom}(Ah)}\int_0^t I(\tau)\ \mathrm{d}\tau \tag{27}$$

assuming the initial state of charge $SOC(t=0)=0$ and $I(t)$ is the applied current with $I>0$ during charge. SOC can be defined as

$$SOC = \frac{\theta_{n,p} - \theta_{0\%}}{\theta_{100\%} - \theta_{0\%}} \tag{28}$$

Using equations (26)–(28), the capacity is defined as

$$C_{nom} = \frac{AF\delta_{n,p}\varepsilon_s^{n,p}c_{s,max}^{n,p}\left[\theta_{100\%}^{n,p} - \theta_{0\%}^{n,p}\right]}{3600}, \quad (\mathrm{Ah}) \tag{29}$$

2.5. Discretization method

The governing PDEs of the ROM constitute the building blocks of the battery model. To be useful for control and systems engineering, the PDEs must be discretized in space to reduce them to coupled multiple ordinary differential equations (ODEs) in the time domain.

2.5.1. Finite difference method

The Finite Difference Method (FDM) is the simplest and the most commonly used approach to the solution of the diffusion equations found in battery models for real-time applications. By using the central finite difference method for the radial dimension r, it is possible to describe the spherical PDE by a set of ordinary differential equations (ODE). Equation (15) can be written as

$$\frac{\partial c_s(r,t)}{\partial t} = D_s\left(\frac{\partial^2 c_s}{\partial r^2} + \frac{2\partial c_s}{r\partial r}\right) \tag{30}$$

By using the CFDM, and discretizing the solid spherical particle into M_r shells along the radial dimension r as shown in Fig. 1, such that $R_s = \Delta r \times (M_r)$, and defining $q = 1, \ldots, M_{r-1}$ equation (30) becomes

Table 1
Final set of reduced-order model equations and underlying assumptions.

Conservation Equation	Assumptions
ROM-Ion concentration in the electrodes	
$\frac{\partial c_s^{n,p}(r,t)}{\partial t} = \frac{D_s}{r^2}\frac{\partial}{\partial r}\left[r^2\frac{\partial c_s^{n,p}(r,t)}{\partial r}\right]$ (15)	Since only one particle is to be considered from the anode and the cathode, the x-dimension has been ignored
$c_e(x,t) = \bar{c}_e$ (16)	The lithium concentration in electrolyte c_e is assumed to be constant, uniform, and equal to an average value
ROM-Ion concentration in the electrolyte	
$\frac{\partial}{\partial x}\left(\sigma^{eff}\frac{\partial}{\partial x}\phi_s(x,t)\right) = \bar{j}_{n,p}^{li}$ (17)	
$\frac{\partial}{\partial x}\left(\kappa^{eff}\frac{\partial}{\partial x}\phi_e(x,t)\right) = -\bar{j}_{n,p}^{li}$ (18)	The lithium concentration in electrolyte c_e is assumed to be constant, uniform, and equal to an average value
ROM-Butler-Volmer kinetics equation	
$\bar{j}_{n,p}^{li} = \frac{I}{A\delta_{n,p}}$ (19)	The lithium concentration in electrolyte c_e is assumed to be constant, and one particle is to be considered from the each electrode. Hence, the spatial dependence of the Butler-Volmer equation is removed

$$\dot{c}_s^{n,p}\Big|_q = \frac{D_s}{\Delta r^2}\left[\left(c_s^{n,p}\Big|_{q+1} - 2c_s^{n,p}\Big|_q + c_s^{n,p}\Big|_{q-1}\right) + \frac{\Delta r}{r_q}\left(c_s^{n,p}\Big|_{q+1} - c_s^{n,p}\Big|_{q-1}\right)\right] \tag{31}$$

By substituting with $r_q = q \times \Delta r$ and rearranging, equation (31) becomes

$$\dot{c}_s^{n,p}\Big|_q = \frac{D_s}{\Delta r^2}\left[\left(\frac{q-1}{q}\right)c_s^{n,p}\Big|_{q-1} - 2c_s^{n,p}\Big|_q + \left(\frac{q+1}{q}\right)c_s^{n,p}\Big|_{q+1}\right] \tag{32}$$

The boundary condition equation (2) can be rewritten accordingly:

$$c_s^{n,p}|_0 = c_s^{n,p}|_1 \tag{33}$$

$$c_s^{n,p}|_{M_r} = c_s^{n,p}\Big|_{M_{r-1}} + \Delta r\frac{-\bar{j}^{li}}{Fa_sD_s} = c_{se}^{n,p} \tag{34}$$

By substituting with the boundary conditions equations (33) and (34), and rearranging, equation (32) becomes

$$\dot{c}_s^{n,p} = \begin{cases} \Psi\left[-2c_s^{n,p}\Big|_q + \left(\frac{q+1}{q}\right)c_s^{n,p}\Big|_{q+1}\right] & : q = 1 \\ \Psi\left[\left(\frac{q-1}{q}\right)c_s^{n,p}\Big|_{q-1} - 2c_s^{n,p}\Big|_q + \left(\frac{q+1}{q}\right)c_s^{n,p}\Big|_{q+1}\right] & : 2 \le q \le M_r - 2 \\ \Psi\left[\left(\frac{q-1}{q}\right)c_s^{n,p}\Big|_{q-1} - \left(\frac{q-1}{q}\right)c_s^{n,p}\Big|_q - \frac{Z}{\Psi}\left(\frac{q+1}{q}\right)\bar{j}^{li}\right] & : q = M_r - 1 \end{cases} \tag{35}$$

where $\Psi = D_s/\Delta r^2$ and $Z = 1/(\Delta r \times a_s \times F)$. The lithium concentration in the solid particle at the outer shell when $r = M_r$ is referred to as the lithium concentration at the solid-electrolyte interface $c_{se}^{n,p}$.

2.5.2. State space representation

With the above approximations for the mass conservation equation and its boundary conditions, a state space representation for equations (31)–(35) can be formulated as follows:

$$\dot{c}_s^{n,p} = \mathbf{A}c_s^{n,p} + \mathbf{B}j^{li} \tag{36}$$

$$c_{se}^{n,p} = c_s^{n,p}|_{M_r} = c_s^{n,p}|_{M_r-1} + \mathbf{D}j^{li} \tag{37}$$

The state space matrices, A, B, and D, are obtained as follows:

$$\mathbf{A} = \Psi\begin{bmatrix} -2 & \frac{q+1}{q} & 0 & \cdots & 0 & 0 \\ \frac{q-1}{q} & -2 & \ddots & & 0 & 0 \\ 0 & \ddots & \ddots & \ddots & & \vdots \\ \vdots & & \ddots & \ddots & \ddots & 0 \\ 0 & 0 & & \ddots & -2 & \frac{q+1}{q} \\ 0 & 0 & \cdots & 0 & \frac{q-1}{q} & -\frac{q-1}{q} \end{bmatrix} \tag{38}$$

$$\mathbf{B} = Z\begin{bmatrix} 0 \\ 0 \\ 0 \\ \vdots \\ \vdots \\ -\frac{q+1}{q} \end{bmatrix} \tag{39}$$

$$\mathbf{D} = -\frac{Z}{\Psi} \tag{40}$$

2.6. Model parameter grouping

The ROM battery voltage equation can be rewritten by substituting equations (21)–(23) in equation (20) as shown below:

$$V(t) = \left[U_p(\theta_p) - U_n(\theta_n)\right] + \vartheta_\eta^{n,p}(\theta_{n,p}, I) - IK_{res} \tag{41a}$$

$$where \quad K_{res} = \frac{1}{A}\left[R_f + \frac{(\delta_n + 2\delta_{sep} + \delta_p)}{2\kappa^{eff}}\right] \tag{41b}$$

where K_{res} is a term that accounts for the increase in ohmic resistance during a charge or discharge current pulse related to the poor electronic conductivity of the cell chemistry.

By substituting $a_s^{n,p} = 3\varepsilon_s^{n,p}/R_s^{n,p}$, and $\alpha_a = \alpha_c = 0.5$ from Table 3, equation (21) can be written as follows:

$$\vartheta_\eta^{n,p}(\theta_{p,n}, I) = \overline{\eta}_p - \overline{\eta}_n = \frac{RT}{\alpha_a F}\ln\frac{\xi_p + \sqrt{\xi_p^2 + 1}}{\xi_n + \sqrt{\xi_n^2 + 1}} \tag{42a}$$

$$where \quad \xi_{n,p} = \Omega^{n,p}\frac{I}{\left(c_{s,\max}^{n,p}c_{se}^{n,p} - c_{se}^{n,p^2}\right)^{0.5}} \tag{42b}$$

$$and \quad \Omega^{n,p} = \frac{R_s^{n,p}}{6A\delta_{n,p}\varepsilon_s^{n,p}(\overline{c}_e)^{0.5}} \tag{42c}$$

where $\Omega^{n,p}$ is a constant term which accounts for the variation of the average electrolyte concentration.

After introducing $\Omega^{n,p}$ and K_{res}, the new set of equations are described in Fig. 3, where the blue-colored constants represent the model parameters.

Equation (35), which describe the lithium-ion concentration in a single spherical particle, are linear time-invariant (LTI). The nonlinearity in the output equation (41) is due to the open circuit

potential term $[U_p(SOC_p) - U_n(SOC_n)]$ and the overpotential difference term $\vartheta_\eta^{n,p}(\theta_{p,n}, I)$. The open circuit potential term is a univariate, nonlinear function of the cell state of charge $U_{n,p}(SOC_{n,p})$. Reducing this term to a CPWL regions while maintaining accuracy aids in reducing the computational complexity of the model.

3. Continuous piecewise linearization

This sections will present the main contribution of this paper, the use of piecewise linearization techniques to reduce the system complexity.

3.1. Background

In the literature, Qingzhi et al. [28] used a cubic spline regression model to fit the experimental open-circuit potential (OCP) curves of two intercalation electrodes of a lithium-ion battery. In this paper, a method is presented for constructing CPWL regions of the experimentally measured OCP data using polynomials of the first order by a stochastic global solution of the resulting mathematical problem. Due to constraints in real time applications, the proposed technique must maintain the continuity and smoothness of the OCP curve at the knot positions.

Pittman et al. [29] have proposed an algorithm that attempts to stochastically find the global solution to an optimization problem that not only minimizes the sum of squared errors (SSE) but also chooses the optimal number of knots that maximizes the information content in each knot. The algorithm proposed in the current work is a modified form of Pittman's algorithm since the optimization problem being solved is more restrictive. First, the number of knots must be known and specified in advance. Second, the knots are not completely free on the fitting interval, but rather are restricted to be unique and in order between the values in the finite set of measurements.

A two-stage framework of knot placement is proposed. We start with an outline of the algorithm, then the knot placement strategy and the genetic algorithm (GA) optimization model are described, respectively.

3.2. Problem formulation and implementation

The open circuit potential as a function of state of charge, $U_{n,p}(SOC_{n,p})$, is a univariate, nonlinear function where $SOC_{n,p} \in [SOC_{n,p}^{0\%}, SOC_{n,p}^{100\%}]$. This nonlinear function has N CPWL functions $\omega_i(\theta)$ within its domain, where λ is a pre-specified number that represents the knot points. Each line segment can be defined as follows:

$$\omega_i(SOC) = \frac{U(\lambda_i) - U(\lambda_{i-1})}{\lambda_i - \lambda_{i-1}}(SOC - \lambda_{i-1}) + U(\lambda_{i-1}) \quad \forall \quad \lambda_{i-1} \leq SOC \leq \lambda_i \tag{43}$$

where λ_i are knot points in $[SOC^{0\%}, SOC^{100\%}]$ and $i = 1, \ldots, N$. The first and the last knot points are fixed at the boundaries, that is, $\lambda_0 = SOC^{0\%}, \lambda_N = SOC^{100\%}$. Also, the knot points are ordered and unique: $\lambda_i > \lambda_{i-1}$ for $i = 1, \ldots, N$. To find the optimal placements for the knot points $\lambda_1, \ldots, \lambda_{n-1}$, such that the overall squared-approximation error *err* is minimized. The optimization objective function is defined as follows:

$$\min_{\lambda_1, \ldots \lambda_{N-1}} \left\{ err = \int_{SOC^{0\%}}^{SOC^{100\%}} [U(SOC) - \omega_i(SOC)]^2 dSOC \right\} \tag{44}$$

The optimization problem can be described as follows:

$$\min_{\lambda_1, \ldots, \lambda_{N-1}} \; err(SOC) \tag{45a}$$

$$s.t. \quad \frac{d}{dSOC}(err(SOC)) = [U(SOC) - \omega_i(SOC)]^2, \quad err\left(SOC^{0\%}\right) = 0 \tag{45b}$$

$$\omega_i(SOC) = \frac{U(\lambda_i) - U(\lambda_{i-1})}{\lambda_i - \lambda_{i-1}}(SOC - \lambda_{i-1}) + U(\lambda_{i-1}) \text{ for } \lambda_{i-1} \leq SOC \leq \lambda_i \tag{45c}$$

$$\lambda_0 = SOC^{0\%}, \quad \lambda_N = SOC^{100\%} \tag{45d}$$

$$\lambda_i \geq \lambda_{i-1} + \varepsilon, \quad i = 1, \ldots, N \tag{45e}$$

The continuity constraint implies that $\omega(\lambda_{i+1}) = \omega(\lambda_i)$, and can be written as:

$$\lambda_i = -\frac{U(\lambda_i) - U(\lambda_{i-1})}{\lambda_i - \lambda_{i-1}}\lambda_{i-1} + U(\lambda_{i-1}) \tag{46}$$

3.3. Optimizing joint-points for continuous piecewise linearization

The proposed method for optimizing the joint-points uses the genetic algorithm (GA), which is inherently stochastic in nature. The GA is theoretically proven to eventually attain global convergence, and its stochastic nature prevents any prediction or calculation of its rate of convergence. As a result, these routines can be computationally expensive in real-time calculations.

Since the continuous piecewise linearization of the OCP will be performed offline, the real-time calculation constraint does not apply. Therefore, the problem can be solved to global optimality by the GA, which guarantees that the resulting solution is globally optimal within an epsilon tolerance.

The experimental procedure for obtaining the OCP curves will be discussed in Section 5. As shown in Fig. 4, the anode OCP is nearly constant. The OCP of the cathode is an order of magnitude higher than that of the anode; therefore, the knot locations are optimized for the cathode. The results of the optimization problem described in equation (44) are shown in equation (47). Since the nonlinear relation between the OCP and the cell SOC is chemistry dependent. The optimized knot locations will differ according to the lithium ion chemistry under consideration. In this experiment, the optimized knot locations are at (6%, 23%, 49%, 78%) SOC_p. Round-off errors at lower SOC are avoided by choosing the first piecewise-linear region interval away from the steep portion of the cathode OCP curve.

$$\lambda = [0.06, 0.23, 0.49, 0.78, 1] \tag{47}$$

Fig. 4 shows the optimized knot locations and compares between the measurement and the piecewise-linear functions. In both parts of the graphs, the x-axis represents the normalized concentration, and the y-axis represents the OCP [V] and residuals [V], in upper and lower figures, respectively. The residuals graph

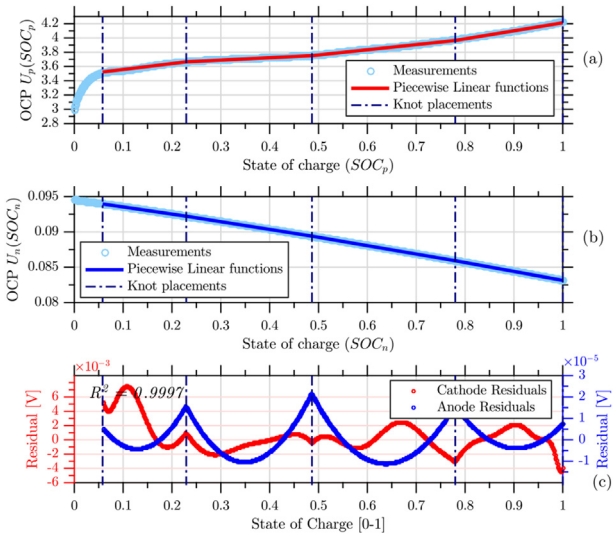

Fig. 4. Comparison of the experimental OCP curves and the CPWL functions obtained by optimizing the joint-points. (a) Cathode, (b) Anode, (c) Residual plot for Cathode (red) and Anode (blue). (For interpretation of the references to colour in this figure legend, the reader is referred to the web version of this article.)

shows the accuracy of the piecewise-linear functions with respect to the nonlinear function; the coefficient of determination of the fitted functions is equal to 0.9997.

By substituting equation (47) in equation (43),

$$\omega(SOC_{n,p}) = \begin{cases} 0.82SOC_p - 0.05SOC_n + 3.42 & : 0.06 \le SOC_p \le 0.23 \\ 0.31SOC_p - 0.05SOC_n + 3.53 & : 0.23 \le SOC_p \le 0.49 \\ 0.69SOC_p - 0.03SOC_n + 3.34 & : 0.49 \le SOC_p \le 0.78 \\ 1.08SOC_p - 0.02SOC_n + 3.09 & : 0.78 \le SOC_p \le 1.00 \end{cases} \quad (48)$$

The CPWL-EAM terminal voltage can be calculated by substituting equations (21), (22) and (48) in equation (20):

$$V(t) = \omega(SOC_{n,p}) + \frac{RT}{\alpha_a F}\ln\frac{\xi_p + \sqrt{\xi_p^2+1}}{\xi_n + \sqrt{\xi_n^2+1}} - IK_{res} \quad (49)$$

3.4. Comparison with existing models

A well-determined model for the nonlinear relation between the OCP and the cell SOC is indispensable for the model performance. The proposed method is compared against six different models summarized by Weng et al. in Ref. [30] and listed in Table 2. The OCP data shown in Fig. 4-a is used to fit the models presented in Table 2 using the Matlab curve fitting toolbox.

The RMS error and CPU time for the models' fitting results are shown in Table 2. The proposed continuous piecewise-linear model has the lowest CPU run time and the third highest accuracy when compared to the other models.

It should be noted that none of the other six models in Table 2 reduces the model to a linear form. The benefit of the piecewise linearization is the ability to incorporate optimal SOC estimation techniques such as Kalman Filter. Linear estimation strategies are simpler, computationally more efficient, more robust and more accurate for linear or piecewise linear systems compared to nonlinear estimation techniques.

Table 3
Model parameters - constant parameters and formula-based parameters.

Symbol	Value		
	Anode	Separator	Cathode
α_a, α_c	0.5	–	0.5
t_0^+	0.363	0.363	0.363
σ	1	–	0.1
σ^{eff}	$\sigma^{eff} = \varepsilon_s^{n,p}\sigma$	–	$\sigma^{eff} = \varepsilon_s^{n,p}\sigma$
$a_s^{n,p}$	$a_s^n = \frac{3\varepsilon_s^{n,p}}{R_s}$	–	$a_s^p = \frac{3\varepsilon_s^{n,p}}{R_s}$
D_e^{eff}	$D_e^{eff} = \varepsilon_e^{1.5} D_e$		
κ	$\kappa = 0.0158 c_e e^{(0.85 c_e^{1.4})}$		
κ^{eff}	$\kappa^{eff} = \varepsilon_s^{n,p}\kappa$		
κ_D^{eff}	$\kappa_D^{eff} = \frac{2RT\kappa^{eff}}{F}(t_0^+ - 1)$		

4. Experimental setup

In this paper, parameterization and validation data sets have been gathered experimentally using a prismatic lithium-ion battery cell suitable for high-power applications like PHEVs, HEV, and EV. The battery positive electrode material is NMC-based, and the anode is graphite-based.

The tests are done on a Scienlab battery test bench. The voltage accuracy is ± 0.05% (≃± 1 mV) of the measured value, the current accuracy is ± 0.05% (≃± 20 mA) of the measured value. The sensors are integrated to the test bench. During testing, the cells are placed in a climate chamber with a continuously controlled ambient temperature of 25° C.

The cycler has 12 channels; four different current profiles were tested on 12 cells (one cell per channel). In order to account for any cell manufacturing variations, each test was conducted on a cluster of three cells of the same type and under the same conditions. The cluster output was averaged to obtain the measurement variables. The cell voltages, currents, and temperature are sampled every 100 ms. The measured variables are used as input data for the presented algorithm in the MATLAB/Simulink environment.

Table 2
Comparison between different open circuit potential models.

#	Model (x = SOC, y = OCP(SOC))	RMSE (mV)	CPU time (ms)	Ref
1	$y = k_0 - \frac{k_1}{x} - k_2 x + k_3 ln(x) + k_4 ln(1-x)$	5.68	0.384	[2]
2	$y = k_0 + k_1(1 - e^{-\alpha_1 * x}) + k_2\left(1 - e^{\frac{-\alpha_2}{1-x}}\right) + k_3 x$	6.40	0.396	[31]
3	$y = k_0 + k_1 e^{-\alpha_1(1-x)} + \frac{k_2}{x}$	3.20	0.226	[32]
4	$y = k_0 + k_1 e^{-\alpha_1 x} + k_2 x + k_3 x^2 + k_4 x^3$	4.69	0.287	[7]
5	$y = k_0 + k_1 x + k_2 x^2 + k_3 x^3 + k_4 x^4 + k_5 x^5 + k_6 x^6$	1.23	0.606	[33]
6	$y = k_0 + k_1\frac{1}{1+e^{\alpha_1(x-\beta_1)}} + k_2\frac{1}{1+e^{\alpha_2(x-\beta_2)}} + k_3\frac{1}{1+e^{\alpha_3(x-1)}} + k_4\frac{1}{1+e^{\alpha_4(x)}} + k_5 x$	1.03	0.960	[30]
7	Continuous Piecewise Linear Model (CPWL), equation (48)	3.16	0.124	

5. Parameter identification procedure

This section presents the procedure for identifying the model parameters. The reduced-order, electrode-averaged model requires fewer parameters than the full-order model; however the number of parameters is still relatively high, if all of the parameters values are considered as unknowns. These parameters represent geometrical, physical, or chemical properties. In order to decrease the number of parameters to be identified, the parameterization process will be divided into two steps.

In step one, the battery cell is operated within [$C/30$ to $C/50$] range of operation using experimental inputs so as to limit the number of parameters which impact the output voltage. The parameters are identified using experimental data. In step two, the battery cell is excited with a signal that is rich in the frequency range necessary to identify the rest of the parameters. This approach has the advantage of providing a trade-off between extensive experimental characterization techniques and purely identifying all of the parameters using nonlinear techniques. Table 3 summarizes the model constants or formula-based parameters [24].

The solid concentrations inside the electrodes and the correlation function between the electrodes' solid concentrations and their OCP are obtained from OCV data. This step relies mostly on utilizing half-cell OCV curves. Next, the rest of parameters are optimized using the GA. Lastly, the model is compared to experimental results.

5.1. Identification of capacity-related parameters

This step identifies the solid concentrations inside the electrodes and is used to obtain the correlation function between the electrodes' solid concentrations and their OCP. This step makes SOC-dependent and rate-dependent parameters easier to identify by sweeping through the full range of battery states of charge at different charge/discharge rates. The correlation between the negative electrode active material solid concentration and its open circuit potential has been measured in the laboratory.

Anode OCP $U_n(\theta_n)$ measurements were made using a composite graphite film ($\simeq$ 140 μm thickness; MTI Corporation) mounted on copper foil in a half-cell versus a solid lithium metal electrode with a standard, commercial electrolyte consisting of 1.0 M LiPF6 in EC/DEC, 1:1 (v/v) (Novolyte Corporation). A coin cell geometry was used, and the cells were assembled under argon atmosphere in a glove box. They were then cycled at C/50 on a BT2000 multi-channel cycler (Arbin Instruments), and the 3rd cycle was used to construct the OCP curve, to allow for SEI formation (Coulombic efficiency was in excess of 99% by this cycle). Both the charge and discharge curves exhibit the characteristic plateaus and stoichiometric phase transitions associated with Li intercalation into graphite, and the inserted and extracted specific capacity is approaching the theoretical specific capacity for graphite of 372 mAh/g as shown in Fig. 5-a.

The Cathode OCP $U_p(\theta_p)$ is calculated by adding the measured battery open circuit voltage V_{ocv} to the Anode OCP $U_n(\theta_n)$.

Table 4
Capacity-related parameters lower and upper bounds.

Symbol	Unit	Anode		Cathode	
		LB	UB	LB	UB
$c_{s,max}^{n,p}$	mol cm^{-3}	$1e^{-4}$	1	$1e^{-4}$	1
$\theta_{0\%}$	–	0	1	0	1
$\theta_{100\%}$	–	0	1	0	1

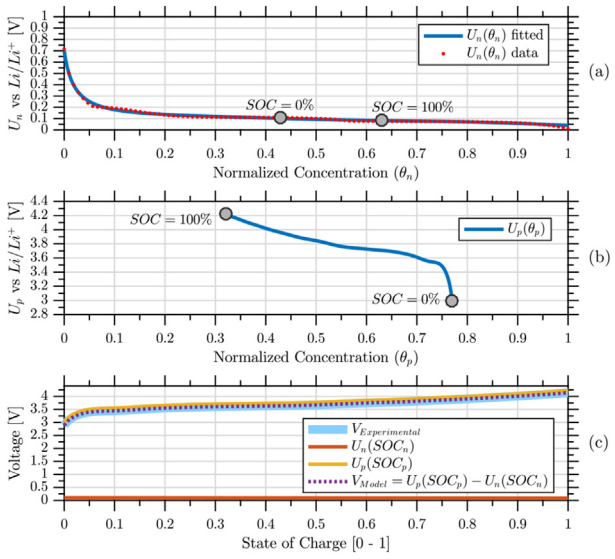

Fig. 5. Open circuit potential versus normalized concentration for (a) positive electrode, (b) negative electrode, and (c) open circuit potentials, experimental versus model.

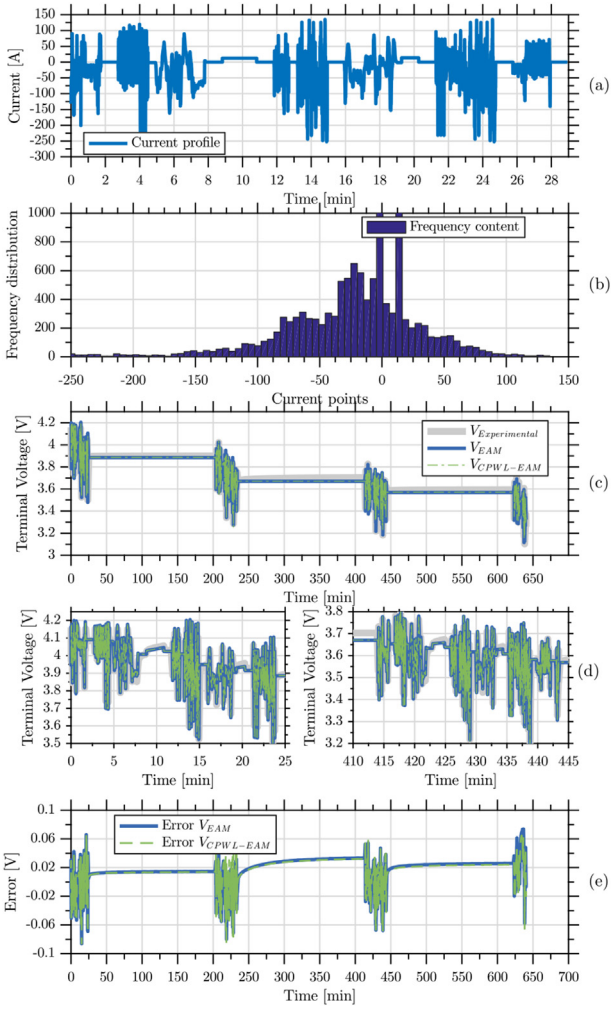

Fig. 6. Parameterization Cycle - (a) Current profile, (b)frequency distribution of the current profile, (c,d) voltage response, and (e) voltage error.

Table 5
Diffusion-related parameters lower and upper bounds.

Symbol	Unit	Anode		Cathode	
		LB	UB	LB	UB
$\epsilon_s^{n,p}$	–	$1e^{-4}$	1	$1e^{-4}$	1
D_e	cm^2s^{-1}	$1e^{-14}$	1	$1e^{-14}$	1
$R_s^{n,p}$	cm	$\frac{\delta_n}{20}$	δ_n	$\frac{\delta_p}{20}$	δ_p
$\overline{c}_e$	mol cm^{-3}	$[1e^{-4} - 1e^{4}]$			
R_f	Ωcm^2	$[1e^{-4} - 1e^{4}]$			
A	cm^2	$[7e^{3} - 9e^{3}]$			

$$U_p(\theta_p) = V_{ocv} + U_n(\theta_n) \tag{50}$$

The obtained Cathode OCP $U_p(\theta_p)$ is shown in Fig. 5-b. The open-circuit potential for the positive electrode $U_p(\theta_p)$ and the negative electrode $U_n(\theta_n)$, along with the OCV (V_{ocv}) relationship are shown in Fig. 5-c. The capacity-related parameters with their lower bounds (LB) and upper bounds(UB) are summarized in Table 4.

5.2. Identification of diffusion-related parameters

The objective of this step is to identify the parameters associated with the battery transient response in each CPWL region. A parameterization cycle that contains charge-sustaining and charge-depleting phases is chosen, as shown in Fig. 6-a. The cycle frequency content makes it easier to identify the cell parameters, as illustrated in Fig. 6-b. The test starts with a fully charged battery and then a current profile is applied to discharge the battery until the SOC specified in equation (47) is reached. Then, the cell is left to rest at this SOC to allow for full cell relaxation. Finally, the cycle is repeated in each CPWL region until the battery is fully discharged.

The diffusion-related parameters, with their lower and upper bounds, are summarized in Table 5. After the identification procedure by the GA, the model shows an accurate voltage prediction, with an approximate Root Mean Square Error (RMSE) of 0.022 [V] and Mean Absolute Error (MAE) of 0.020 [V]. The identified parameter set is listed in Table 6.

Under the parameterization cycle, the model shows an accurate voltage prediction during both the steady and transient phases, as shown in Fig. 6-c and 6-d. The gray-solid line represents the experimental battery voltage, while the blue-solid and green-dotted lines represent the EAM and CPWL-EAM responses, respectively. The lower part of the figure shows the error between the measured voltage and the calculated voltage of the models. Since the error is determined by subtracting the measured voltage from the estimated voltage; the positive error implies under-

Table 6
Identified model parameters.

Symbol	Unit	Identified values	
		Anode	Cathode
$c_{s,max}^{n,p}$	mol cm^{-3}	0.072	0.080
$\theta_{0\%}$	–	0.428	0.824
$\theta_{100\%}$	–	0.774	0.483
$\epsilon_s^{n,p}$	–	0.958	0.950
$R_s^{n,p}$	cm	0.00026	0.000475
A	cm^2	8833.9	
$\overline{c}_e$	mol cm^{-3}	[3.13, 3.11, 3.11, 2.07]× 1e2	
R_f	Ωcm^2	[1.73, 1.93, 1.97, 2.81]× 1e-7	
D_e^n	cm^2s^{-1}	[7.45, 7.45, 7.45, 7.45]× 1e-10	
D_e^p	cm^2s^{-1}	[8.43, 7.38, 5.21, 4.87]× 1e-10	

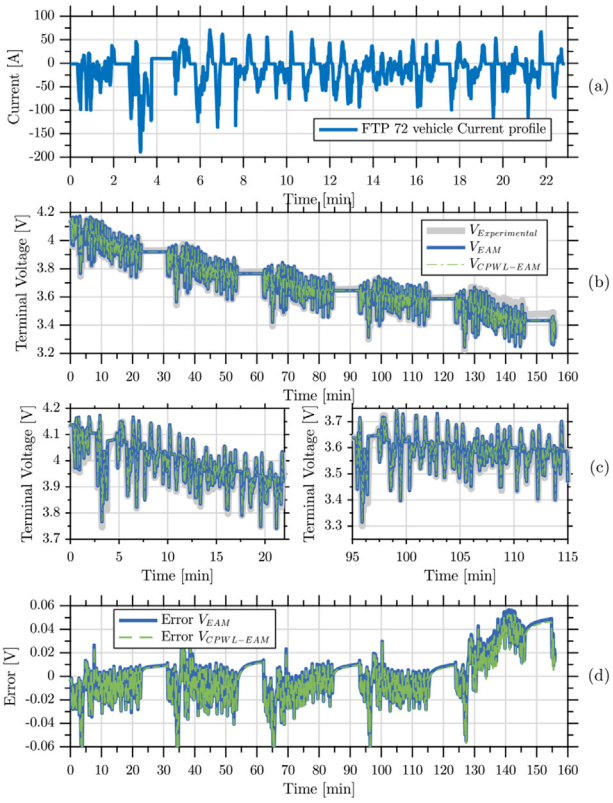

Fig. 7. Validation Cycle (FTP72) - (a) Current profile, (b,c) voltage response, and (d) voltage error.

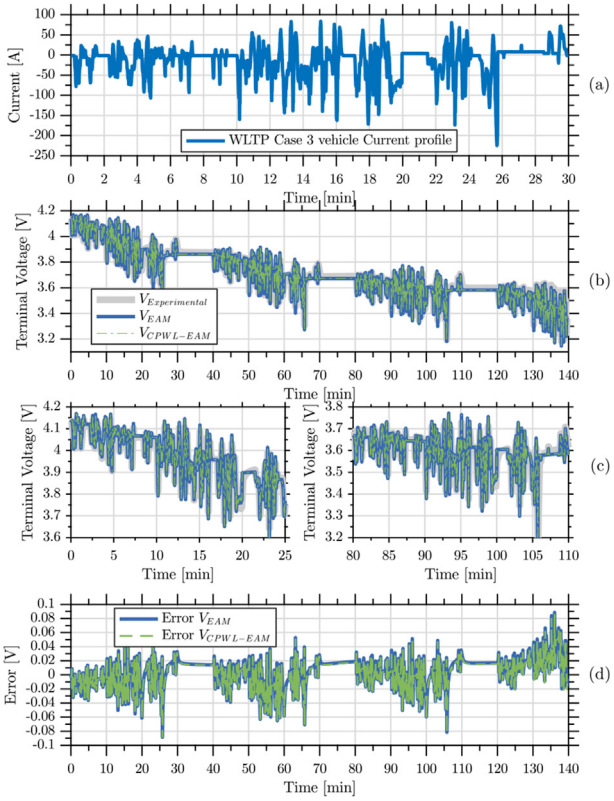

Fig. 8. Validation Cycle (WLTP- case 3) - (a) Current profile, (b,c) voltage response, and (d) voltage error.

Table 7
Model results for different cycles (a) RMSE and MAE [V], (b) Computation time [sec].

a	EAM		CPWL-EAM	
	RSME	MAE	RSME	MAE
Parameterization cycle	0.023	0.021	0.022	0.020
Validation cycle - FTP72	0.020	0.015	0.019	0.014
Validation cycle - WLTP	0.019	0.015	0.018	0.015
Mean	0.020	0.017	0.020	0.016

b	EAM CPU time (sec)	CPWL-EAM CPU time (sec)
Parameterization cycle	4.23	3.82
Validation cycle - FTP72	1.11	1.02
Validation cycle - WLTP	1.01	0.09
Mean	2.12	1.64

calculation, while the negative error indicates over-calculation.

6. Model validation under different driving profiles

In this section, the model performance is compared with experimental data to demonstrate the effectiveness of the preceding methodology. The validation cycles in this section are different from those utilized for the purpose of identification. The two validation cycles used are the US Federal Test Procedure (FTP-72) cycle, also called the Urban Dynamometer Driving Schedule (UDDS), and the Worldwide Harmonized Light Vehicles Test Procedure (WLTP). The two error quantitative matrices are the RMSE and MAE.

6.1. Results under FTP72

The first set of validation data is the FTP-72 cycle as shown in Fig. 7-a. Under the FTP-72 cycle, the calculated voltages of the EAM and the CPWL-EAM are compared against the measured voltage in Fig. 7-b and 7-c, with the voltage error shown in Fig. 7-d. The gray-solid line represents the experimental battery voltage, while the blue-solid and green-dotted lines represent the EAM and CPWL-EAM responses, respectively. The RMSE between the modeled voltage and the measured voltage over five consecutive cycles with 10 min rest between cycles is 0.019 V, and the MAE is 0.014 V.

6.2. Results under WLTP-Case 3

The second set of validation data is Case 3 of the WLTP. Case 3 stands for high-power vehicles with Power to Weight ratio (PWr) $>$ 34. This driving cycle consists of four parts Low, Medium, High, and Extra High-speed as shown in Fig. 8-a.

Under the WLTP cycle, the calculated voltages of the EAM and the CPWL-EAM are compared against measured voltage in Fig. 8-b and 8-c with the voltage error shown in Fig. 8-d. Here again, The gray-solid line represents the experimental battery voltage, while the blue-solid and green-dotted lines represent the EAM and CPWL-EAM responses, respectively. The RMSE between the modeled voltage and the measured voltage over four consecutive cycles with 10 min rest between cycles is 0.018 V, and the MAE is 0.015 V.

7. Results and comparison

By comparing the voltage error under the various different discharge currents in Figs. 6-c, 7-b, and 8-b, it is clear that the CPWL-EAM exhibits accurate voltage prediction during the steady and transient phases of cycling. The proposed model was able to maintain the voltage prediction accuracy, while decreasing the mean CPU time as shown in Table 7. The reduction in the CPU runtime by around 20% (from 2.12 s to 1.64 s), due to the reformulation of the nonlinear OCP equation as a four-point lookup table, where the voltage values falling between the points are calculated using onboard linear interpolation. The CPU times presented in this publication were run on a 2.30 GHz Intel processor with 16 GB RAM.

8. Conclusion

In conclusion, a continuous, piecewise-linear, electrode-average model is presented, which exhibits high accuracy and reduced CPU runtime compared with the reduced-order, electrode-average model (EAM). The proposed CPWL-EAM linearizes the univariate, nonlinear relation between the OCP and the cell SOC, while maintaining the continuity and smoothness of the OCP curve. The piecewise-linear regions were identified using a novel optimal knot-placement technique which uses GA to determine the optimal knot-locations, while maintaining the continuity constraints. The model is parametrized using a new technique that provides a trade-off between extensive experimental characterization techniques and purely identifying all parameters using nonlinear techniques. The accuracy of the CPWL-EAM is validated through comparison with experimental data and the EAM under the real-time driving profiles FTP-72 and WLTP. The calculated RMSE and MAE are 0.020 V and 0.016 V respectively. Since the CPWL-EAM model shows accurate voltage prediction, while reducing the running time by 20%, the proposed model can be easily implemented on-board in a real-time BMS. Future work will focus on incorporating optimal state of charge estimation techniques (e.g. Kalman Filter), along with model parameterization and validation under different temperature and aging conditions through changing of the knot-location.

Acknowledgment

This research was funded by the Natural Sciences and Engineering Research Council of Canada (NSERC) and BMW AG under grant number CRDPJ 452271-13 and Ontario Centers of Excellence (OCE) TalentEdge Program under grant number OCE24309. The authors would like to thank David Bazak for performing half-cell measurements, and proofreading the manuscript.

Nomenclature

Acronyms

A	State matrix in linear state model state equation, –
B	Input matrix in linear state model state equation, –
D	Input matrix in linear state model output equation, –
A	Electrode plate Area, cm^2
a_s	Active surface area per electrode unit volume, $cm^2 cm^{-3}$
c	Concentration of lithium ions, mol cm^{-3}
D	Diffusion coefficient of lithium species, $cm^2 s^{-1}$
F	Faraday's Constant (F = 96,487), C mol^{-1}
I	Applied current, A
j^{li}	Butler-Volmer current density, A cm^{-3}
q	Discretization step, –
R	Universal gas constant (R = 8.3143), J $mol^{-1}K^{-1}$
r	Radial coordinate, cm
R_f	Film resistance on the electrodes surface, Ωcm^2
$R_s^{n,p}$	Solid active material particle radius, cm
T	Absolute Temperature, K
t	Times

t_0^+ Transference number of lithium ion, –
x Cartesian coordinate, s

Greek Symbols

α_a, α_c Anodic and cathodic charge transfer coefficients, –
δ Thickness, cm
η Surface overpotential of an electrode reaction, V
κ Electrolyte phase ionic conductivity, $\Omega^{-1}cm^{-1}$
κ_D Electrolyte phase diffusion conductivity, $\Omega^{-1}cm^{-1}$
ϕ Volume averaged electrical potential, V
σ Conductivity of solid active material, $\Omega^{-1}cm^{-1}$
θ Reference stoichiometry, –
ϵ_e Electrolyte phase volume fraction, –
ϵ_s Active material volume fraction, –

Superscripts

eff Effective, –
n Anode, –
p Cathode, –
sep Separator, –

Subscripts

e Electrolyte phase, –
s Solid phase, –

References

[1] L. Lu, X. Han, J. Li, J. Hua, M. Ouyang, A review on the key issues for lithium-ion battery management in electric vehicles, J. power sources 226 (2013) 272–288.
[2] G.L. Plett, Extended kalman filtering for battery management systems of lipb-based hev battery packs: Part 1. background, J. Power sources 134 (2) (2004) 252–261.
[3] G.L. Plett, Extended kalman filtering for battery management systems of lipb-based hev battery packs: Part 2. modeling and identification, J. power sources 134 (2) (2004) 262–276.
[4] G.L. Plett, Extended kalman filtering for battery management systems of lipb-based hev battery packs: Part 3. state and parameter estimation, J. power sources 134 (2) (2004) 277–292.
[5] M. Farag, S. Gadsden, S. Habibi, J. Tjong, A comparative study of li-ion battery models and nonlinear dual estimation strategies, in: 2012 IEEE Transportation Electrification Conference and Expo (ITEC), IEEE, 2012, pp. 1–8.
[6] B. Schweighofer, K.M. Raab, G. Brasseur, Modeling of high power automotive batteries by the use of an automated test system, Instrum. Meas. IEEE Trans. 52 (4) (2003) 1087–1091.
[7] M. Chen, G. Rincón-Mora, et al., Accurate electrical battery model capable of predicting runtime and iv performance, Energy Convers. IEEE Trans. 21 (2) (2006) 504–511.
[8] M.W. Verbrugge, R.S. Conell, Electrochemical and thermal characterization of battery modules commensurate with electric vehicle integration, J. Electrochem. Soc. 149 (1) (2002) A45–A53.
[9] Mohammed Farag, Matthias Fleckenstein, Saeid R. Habibi, Li-ion Battery SOC Estimation Using Non-linear Estimation Strategies Based on Equivalent Circuit Models, 2014. SAE Technical Paper, SAE International.
[10] M. Doyle, T.F. Fuller, J. Newman, Modeling of galvanostatic charge and discharge of the lithium/polymer/insertion cell, J. Electrochem. Soc. 140 (6) (1993) 1526–1533.
[11] T.F. Fuller, M. Doyle, J. Newman, Simulation and optimization of the dual lithium ion insertion cell, J. Electrochem. Soc. 141 (1) (1994) 1–10.
[12] V.R. Subramanian, V.D. Diwakar, D. Tapriyal, Efficient macro-micro scale coupled modeling of batteries, J. Electrochem. Soc. 152 (10) (2005) A2002–A2008.
[13] V.R. Subramanian, V. Boovaragavan, V.D. Diwakar, Toward real-time simulation of physics based lithium-ion battery models, Electrochem. Solid-State Lett. 10 (11) (2007) A255–A260.
[14] V.R. Subramanian, V. Boovaragavan, V. Ramadesigan, M. Arabandi, Mathematical model reformulation for lithium-ion battery simulations: galvanostatic boundary conditions, J. Electrochem. Soc. 156 (4) (2009) A260–A271.
[15] L. Cai, R.E. White, Reduction of model order based on proper orthogonal decomposition for lithium-ion battery simulations, J. Electrochem. Soc. 156 (3) (2009) A154–A161.
[16] J.C. Forman, S. Bashash, J.L. Stein, H.K. Fathy, Reduction of an electrochemistry-based li-ion battery model via quasi-linearization and padé approximation, J. Electrochem. Soc. 158 (2) (2011) A93–A101.
[17] C. Wang, W. Gu, B. Liaw, Micro-macroscopic coupled modeling of batteries and fuel cells i. model development, J. Electrochem. Soc. 145 (10) (1998) 3407–3417.
[18] K.A. Smith, C.D. Rahn, C.-Y. Wang, Model order reduction of 1d diffusion systems via residue grouping, J. Dyn. Syst. Meas. Control 130 (1) (2008) 011012.
[19] K. Smith, C.D. Rahn, C.-Y. Wang, et al., Model-based electrochemical estimation and constraint management for pulse operation of lithium ion batteries, Control Syst. Technol. IEEE Trans. 18 (3) (2010) 654–663.
[20] B. Bhikkaji, T. Söderström, Reduced order models for diffusion systems using singular perturbations, Energy Build. 33 (8) (2001) 769–781.
[21] M. Golubitsky, I. Stewart, et al., Singularities and Groups in Bifurcation Theory, vol. 2, Springer Science & Business Media, 2012.
[22] B.S. Haran, B.N. Popov, R.E. White, Determination of the hydrogen diffusion coefficient in metal hydrides by impedance spectroscopy, J. Power Sources 75 (1) (1998) 56–63.
[23] S. Santhanagopalan, Q. Guo, P. Ramadass, R.E. White, Review of models for predicting the cycling performance of lithium ion batteries, J. Power Sources 156 (2) (2006) 620–628.
[24] D. Di Domenico, A. Stefanopoulou, G. Fiengo, Lithium-ion battery state of charge and critical surface charge estimation using an electrochemical model-based extended kalman filter, J. Dyn. Syst. Meas. control 132 (6) (2010) 061302.
[25] S.K. Rahimian, S. Rayman, R.E. White, Extension of physics-based single particle model for higher charge–discharge rates, J. Power Sources 224 (2013) 180–194.
[26] D.D. Domenico, G. Fiengo, A. Stefanopoulou, Lithium-ion battery state of charge estimation with a kalman filter based on a electrochemical model, in: Control Applications, 2008. CCA 2008. IEEE International Conference on, IEEE, 2008, pp. 702–707.
[27] G.K. Prasad, C.D. Rahn, Model based identification of aging parameters in lithium ion batteries, J. power sources 232 (2013) 79–85.
[28] Q. Guo, R.E. White, Cubic spline regression for the open-circuit potential curves of a lithium-ion battery, J. Electrochem. Soc. 152 (2) (2005) A343–A350.
[29] J. Pittman, Adaptive splines and genetic algorithms, J. Comput. Graph. Statistics 11 (3) (2002) 615–638.
[30] C. Weng, J. Sun, H. Peng, An open-circuit-voltage model of lithium-ion batteries for effective incremental capacity analysis, in: ASME 2013 Dynamic Systems and Control Conference, American Society of Mechanical Engineers, 2013. V001T05A002–V001T05A002.
[31] Y. Hu, S. Yurkovich, Y. Guezennec, B. Yurkovich, Electro-thermal battery model identification for automotive applications, J. Power Sources 196 (1) (2011) 449–457.
[32] D. Neumann, S. Lichte, A.M.-D. B.D., Model, with thermal feedback applied to a lithium-ion battery pack, in: NDIA Ground Vehicle Systems Engineering and Technology Symposium-modeling & Simulation, Testing and Validation (MSTV) Mini-symposium, 2011.
[33] A. Szumanowski, Y. Chang, Battery management system based on battery nonlinear dynamics modeling, IEEE Trans. Veh. Technol. 57 (3) (2008) 1425–1432.